Distributed quantum sensing with modeentangled spin-squeezed atomic states

https://doi.org/10.1038/s41586-022-05363-z

Benjamin K. Malia^{1,2,5}, Yunfan Wu^{3,5}, Julián Martínez-Rincón^{1,4} & Mark A. Kasevich^{1,3 ⊠}

Received: 12 May 2022

Accepted: 16 August 2022

Published online: 23 November 2022



Check for updates

Quantum sensors are used for precision timekeeping, field sensing and quantum communication¹⁻³. Comparisons among a distributed network of these sensors are capable of, for example, synchronizing clocks at different locations⁴⁻⁸. The performance of a sensor network is limited by technical challenges as well as the inherent noise associated with the quantum states used to realize the network9. For networks with only spatially localized entanglement at each node, the noise performance of the network improves at best with the square root of the number of nodes¹⁰. Here we demonstrate that spatially distributed entanglement between network nodes offers better scaling with network size. A shared quantum nondemolition measurement entangles a clock network with up to four nodes. This network provides up to 4.5 decibels better precision than one without spatially distributed entanglement, and 11.6 decibels improvement as compared to a network of sensors operating at the quantum projection noise limit. We demonstrate the generality of the approach with atomic clock and atomic interferometer protocols, in scientific and technologically relevant configurations optimized for intrinsically differential comparisons of sensor outputs.

Distributed quantum sensors detect and compare phase shifts between spatially distinct modes of quantum systems with high precision⁴⁻⁶. For example, the gravitational potential can induce relative phase shifts between spatially separated atomic clocks¹ or atom interferometers¹¹. Quantum systems are an attractive platform for networks as they have the unique ability to directly benefit from both spatially localized and spatially distributed entanglement. Experiments have demonstrated entanglement-enhanced networks in both discrete¹² and continuous variable¹³ configurations. In general, quantum networks will have an important role in future technologies. Substantial progress has been made with networks of quantum systems^{2,7,14–18} for enhanced communication^{19,20} and timekeeping^{21,22} at the global scale.

At small length scales, optical atomic clocks have pushed precision to record levels. In one work¹⁰, up to six multiplexed Sr atomic clocks spaced over 1 cm are implemented to achieve a fractional frequency precision at the 10⁻²⁰ level. Another work⁸ has measured the gravitational redshift over 1 mm within a single, spatially distributed sample of atomic Sr. In these systems, the precision of each clock is limited by the quantum projection noise (QPN) limit. In these mode-separable systems, the absence of spin correlations between the spatial modes causes the total precision to scale as $1/\sqrt{M}$ where M is the number of identical clocks being compared.

Through entanglement, a spin-squeezed clock or sensor is able to achieve precision beyond the QPN limit 9,23. However, if a network of squeezed clocks is mode separable, then the total precision still scales as $1/\sqrt{M}$. If spatially distributed entanglement does exist, then the total precision of such a mode-entangled system has the potential to scale with the Heisenberg limit, 1/M (refs. $^{21,22,24-26}$). This scaling in a photonic system has been demonstrated³, and it has been measured in a system of two Sr⁺ ions connected by a photonic link²⁷. Our work addresses a spin-squeezed 87Rb mode-entangled network, the noise of which scales better than a mode-separable network.

Several methods exist for generating spin-squeezing between spatially separate modes. In a pioneering work²⁸, two spatially separated Rb vapour cells were probed via a photonic quantum nondemolition (QND) measurement. In Bose–Einstein condensates, on the other hand, spin-squeezing can be generated through spatially localized collisions before the state is allowed to expand to several micrometers²⁹⁻³¹. Each part of the cloud can then be imaged separately. More recently, another work separated an entangled Bose-Einstein condensate state even further, to 80 µm, with the application of velocity-dependent Raman transitions³². Not only does the spin system now occupy separate spatial modes, but the modes consist of states with differing momenta. Finally, atom-cavity interactions can entangle two momentum states with different spin states³³.

In this work we demonstrate a spatially distributed multimode atomic clock network with noise below the QPN limit. Velocity-dependent Raman transitions create up to four spatial modes (each separated from an adjacent mode by approximately 20 µm) before a spatially distributed QND measurement is performed to entangle the spins of the modes. This entanglement enhances the precision of the frequency comparison within networks of identical clocks, each containing 45,000 atoms per mode. A mode-entangled four-mode network exhibits noise roughly 4.5(0.8) dB lower than that of an equivalent

Department of Physics, Stanford University, Stanford, CA, USA, 2School of Applied and Engineering Physics, Cornell University, Ithaca, NY, USA, 3Department of Applied Physics, Stanford University, Stanford, CA, USA. 4Present address: Quantum Information Science and Technology Laboratory, Instrumentation Division, Brookhaven National Laboratory, Upton, NY, USA ⁵These authors contributed equally: Benjamin K. Malia and Yunfan Wu. [™]e-mail: kasevich@stanford.edu

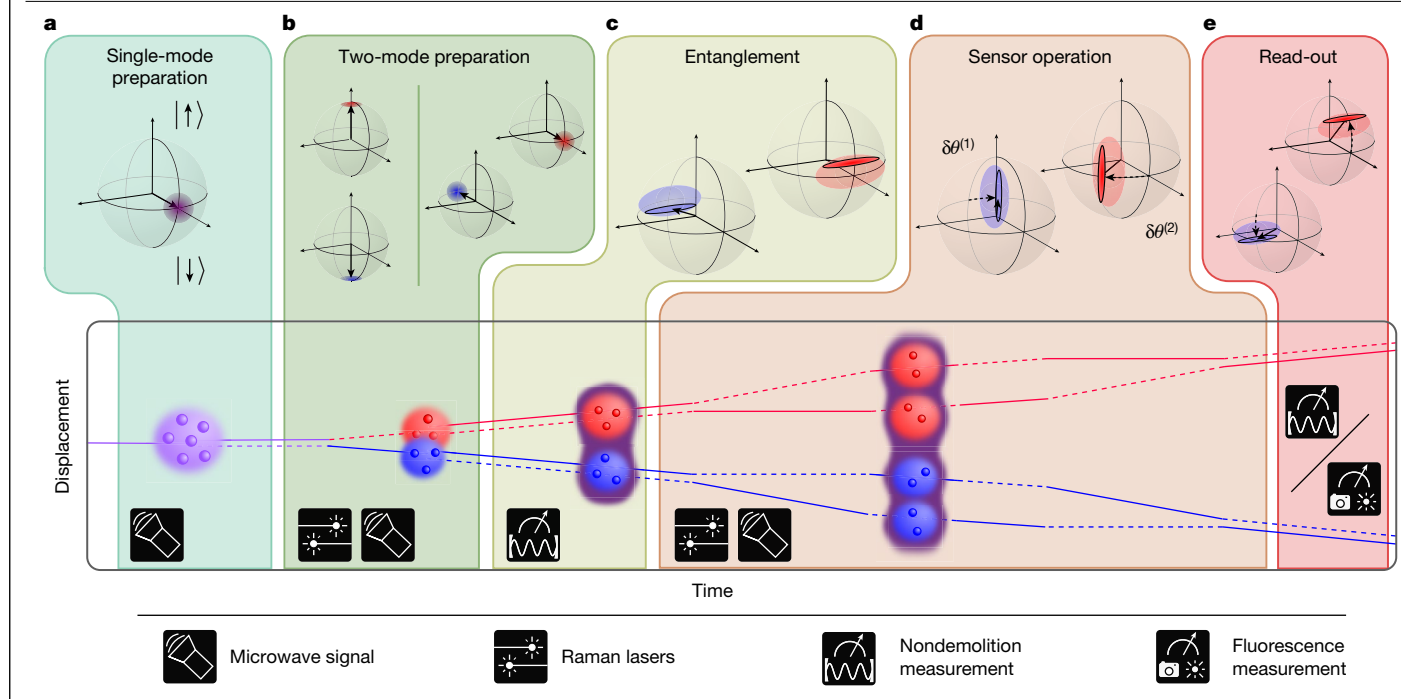


Fig. 1|**Atomic sensor sequence. a**, Single-mode preparation: a localized ensemble of atoms (purple circles) is prepared in a $\langle J_z \rangle$ = 0 CSS. The purple distribution on the Bloch sphere is the Wigner function of the CSS with a variance of N/4. **b**, Two-mode preparation: counter-propagating Raman lasers split the ensemble into two spatially distinct modes (red and blue circles). Each mode's spin is located opposite each other on their respective Bloch spheres (red and blue distributions). We note that because the spatial modes are separable here, the two distributions are not dependent on each other. At this stage, a $\pi/2$ microwave pulse brings both of these states to $\langle J_z \rangle$ = 0. **c**, Entanglement: a probe laser performs a QND measurement to create spin-squeezing (represented by purple shadows). Measuring each mode independently does not give enhanced precision on the total measurement (grey shaded distribution represents the CSS of each mode). To show how simultaneous measurement improves precision, an example of marginal

(light distributions) and conditional (black outlined distributions) Wigner functions 45 are shown on the Bloch spheres. Here the red mode squeezed above the equator is conditional on the blue mode being found below the equator. \mathbf{d} , Sensor operation: the sensor requires an initial application of a $\pi/2$ microwave pulse, which rotates the SSS to a vertical (phase sensitive) orientation on the Bloch sphere. The observable that is being measured dictates the series of microwave and Raman pulses applied during the sensor sequence. The atomic interferometer sequence is pictured, with a detailed description of its sequence described in Extended Data Fig. 3. Mean trajectories of spin down (up) states are represented by solid (dotted) lines. (Relative times are not to scale). In the presence of a field gradient, the phases of the modes shift by $\delta\theta^{(m)}$ (dashed arrows). \mathbf{e} , Read-out: a $\pi/2$ microwave pulse then rotates the states back to a horizontal orientation and a second measurement (either QND or fluorescence population spectroscopy) is performed to measure the shift in the sum of all spin values.

mode-separable network of spin-squeezed states (SSS) and 11.6(1.1) dB lower than a network of coherent spin states (CSS) operating at the QPN limit (numbers in parentheses represent one standard deviation). Finally, we employ an M=2 node network to demonstrate an entangled differential atom interferometer.

QND measurements

The methods and apparatus used to generate and detect SSS are detailed in refs. 34,35 . In summary, ensembles of up to 220,000 87 Rb atoms are cooled to 25 μ K and trapped in a 1,560-nm one-dimensional lattice within a dual wavelength optical cavity (see Extended Data Fig. 1). This cavity enables QND measurements via a 780-nm probe detuned from the D_2 transition. These projective measurements detect and squeeze the collective spin of the ensemble, $J_z = (N_{\uparrow} - N_{\downarrow})/2$, where N_i are the populations of atoms in each state after the measurement. This spin-1/2 system is defined by the hyperfine ground states of 87 Rb, $|\downarrow\rangle = 5^2 S_{1/2} |F = 1$, $m_F = 0$ and $|\uparrow\rangle = 5^2 S_{1/2} |F = 2$, $m_F = 0$.

To generate spatially separate modes, velocity-dependent stimulated Raman transitions couple these spin states to momentum ${\bf p}$, where eigenstates are denoted as |spin, ${\bf p}$ ⟩. The relevant transitions are driven by ${\bf \pi}$ pulses that take $|\downarrow,{\bf p}_i\rangle \rightarrow |\uparrow,{\bf p}_i+2\hbar{\bf k}\rangle$ and $|\uparrow,{\bf p}_i\rangle \rightarrow |\downarrow,{\bf p}_i-2\hbar{\bf k}\rangle$, where ${\bf k}$ is the difference between the wavevectors of each of the counterpropagating beams (effective wavevector) associated with the Raman transition. Without loss of generality, the initial

momentum \mathbf{p}_i can be set to zero. A laser system drives Raman transitions between ground-state hyperfine levels (see Methods). The π pulse time is short enough to address nearly the entire velocity distribution of the atom source (the linewidth of the Raman transition is larger than the Doppler width). The transitions occur with a Rabi frequency of $\Omega_R = 2\pi \times 500$ kHz, and the maximum transition probability for a single Raman π pulse is 88%.

When a spin state in an equal superposition of $|\downarrow,0\rangle$ and $|\uparrow,0\rangle$ experiences a Raman π pulse, it coherently evolves into a linear superposition of the two momentum modes $|\uparrow,+2\hbar\mathbf{k}\rangle$ and $|\downarrow,-2\hbar\mathbf{k}\rangle$ (see Fig. 1b). To determine the coherence between the two modes, we apply a second Raman π pulse a time T after the first Raman pulse such that the states have drifted apart by a distance $v_{\rm rel}T$, where $v_{\rm rel}=4\hbar|\mathbf{k}|/m_{\rm Rb}=2.4~{\rm cm~s^{-1}}$ is the relative velocity induced by the stimulated Raman interaction and $m_{\rm Rb}$ is the mass of an atom. A final microwave $\pi/2$ pulse is then used to probe the coherence between the two modes (the microwave Rabi frequency is approximately $2\pi \times 3$ kHz here and in the work described below). As T increases, the coherence is observed to decay as $e^{-T/\beta}$ with a time constant $\beta=0.46~\mu$ s, owing to the velocity spread (approximately $6.9~{\rm cm~s^{-1}}$) of the atomic source (see Methods). After roughly $T=1.5~\mu$ s (36 nm of separation) the contrast becomes negligible, indicating mode separation.

If no effort is made to coherently recombine these momentum modes, the system can now be treated as a two-mode quantum network, where each spatial mode m has a collective spin length of $(J_x^{(m)})^2 = N^{(m)}/2$ and a QPN limited variance $(\Delta J_z^{(m)})^2 = N^{(m)}/4$. Modes with

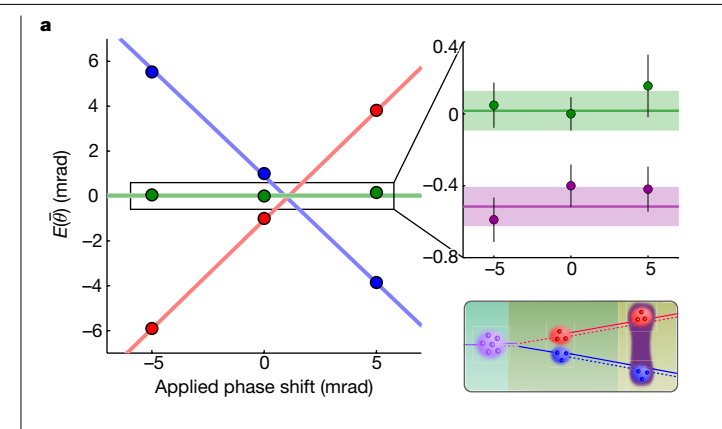
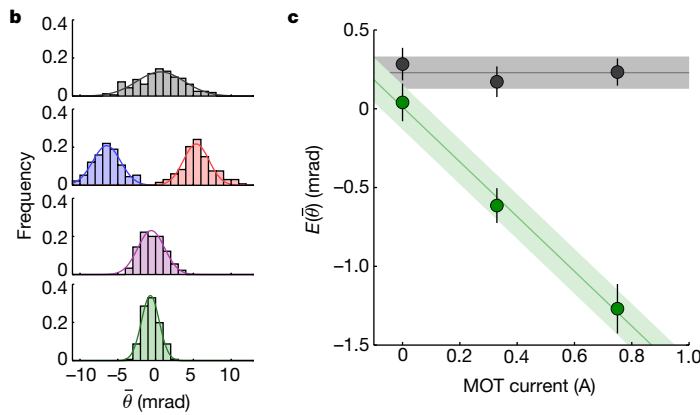


Fig. 2 | Differential phase shift detection. a, For the two-mode case depicted in the space-time diagram, the expected value of $\bar{\theta}$ is measured after the final microwave pulse is phase shifted. Solid lines are linear fits to the expected values for the N = 80,000 positive momentum mode (blue), N = 80,000negative mode (red), and N = 40,000 mode-entangled (green) cases. $\overline{\theta}$ in the single-mode cases are offset by 1 and -1 mrad, respectively, for visual clarity. The enlarged region contains the average of the single momentum modes, that is, mode-separable states (purple), which are offset by -0.4 mrad for visual clarity. In all subfigures, error bars represent the standard error of the mean (SEM) for a set of 200 samples and shaded areas represent 68% confidence



intervals of the fits. **b**, Distributions of 200 sample measurements for the two-mode sensor with coherent states (black), single-mode states (blue and red), mode-separable states (purple) and mode-entangled states (green). Corresponding curves are Gaussian fits. c, Response of a two-mode, modeentangled sensor to a magnetic field gradient applied in the second half of the echo sequence (green circles). For reference, when the sensor sequence's microwave pulses are not performed (black circles), there is negligible change in $\overline{\theta}$ as the applied field increased. The relative magnetic field strength was determined by the relative voltage applied to the MOT coils.

nearly equal mean atom number N can each be represented on composite Bloch spheres with radii CN/2, where the contrast C = 78(3)% is determined by fluorescence imaging. Spin-squeezing improves the measurement of a linear combination of the polar angle shifts $\delta\theta^{(m)} = \delta J_z^{(m)}/(CN/2)$, where $\delta J_z^{(m)}$ are the differences in spin values between a first and second measurement (see Fig. 1). In the remainder of this work the measurable quantity $\overline{\theta}$, determined from the shift in the squeezed collective $\delta J_z = \sum \delta J_z^{(m)}$ value, will refer to the mean of the angles,

$$\overline{\theta} = \frac{1}{M} \sum_{m=1}^{M} \delta \theta^{(m)} = \frac{1}{CMN/2} \sum_{m=1}^{M} \delta J_z^{(m)},$$
 (1)

and $\Delta \bar{\theta}$ to the square root of its variance. The second observation of the collective *I*, is accomplished with a second cavity OND measurement in the case of a clock network demonstration (following ref. 34) or a precision fluorescence measurement in the case of an atom interferometer demonstration (following ref. 35).

To first demonstrate the effect of phase shifts on each spatial mode, ensembles of 80,000 atoms are prepared in three different initial states: $|\uparrow, 2\hbar \mathbf{k}\rangle$, $|\downarrow, -2\hbar \mathbf{k}\rangle$ or a superposition of the two (the atom number differs between the modes by about 1% in the third case, owing to imperfections in the separating π pulse, as measured by the QND pulse). In the superposition case, waiting 0.9 ms separates the modes by roughly 20 μm, a much greater distance than the 36-nm coherence length identified above. The spins of the two modes now point towards opposite poles on their respective Bloch spheres. As shown in Fig. 1, a $\pi/2$ microwave pulse is then applied to the atoms. The pulse brings their vectors to the equator of their Bloch spheres (with radius 20,000 in the third case). The mode with positive momentum, for example, is now in a superposition of $|\downarrow, 2\hbar \mathbf{k}\rangle$ and $|\uparrow, 2\hbar \mathbf{k}\rangle$. Because the microwave $\pi/2$ pulse simultaneously addresses both modes, the Bloch vectors remain anti-parallel. Finally, a (now spatially distributed) QND measurement is performed to projectively squeeze the distributed states²² (with a maximum variance of 9.5(0.5) dB below the QPN limit). This operation leads to a spatially distributed spin correlation of J_z values between the modes while increasing the variance of the spin distributions in the $J_x - J_y$ plane, as illustrated in Fig. 1.

Once the mode-entangled state has been prepared, a microwave $\pi/2-\pi-\pi/2$ spin echo sequence with T_{int} = 110 μ s between each pulse is performed. The phases of the microwave pulses are adjusted to accommodate the a.c. Stark shift (approximately 1 rad) induced by the entangling QND pulse so that the J_z distributions are in metrologically sensitive configurations, as illustrated in Fig. 1. This is accomplished through observation of J_z for the independently prepared momentum modes $|\uparrow, 2\hbar \mathbf{k}\rangle$ and $|\downarrow, 2\hbar \mathbf{k}\rangle$. A second QND measurement determines the phase shift applied to the last microwave pulse. The two single-mode cases, $\overline{\theta} = \delta \theta^{(1)}$, experience nearly equal and opposite responses owing to their anti-parallel spins (see Fig. 2a,b). $\bar{\theta}$ in the mode-entangled case is consistent with the mean of the single-mode cases, indicating that each mode reacts oppositely to the applied shift. Therefore, a sensor utilizing this method will suppress phase noise associated with the pulses used for coherent spin manipulation. This property is useful for suppressing oscillator noise in clock comparisons and optical phase noise in light-pulse atom interferometry applications (as demonstrated below).

On the other hand, this type of sensor will measure a differential phase shift between the two spatial modes due to, for example, position-dependent fields³⁶. We demonstrate a nonzero differential measurement via the application of a magnetic field gradient across the 20-µm separation between the two modes. To introduce a clock frequency imbalance between the two modes, the magnetic field coils of the magneto-optical trap (MOT) are pulsed on during the second half of the echo sequence. As the magnetic field gradient (determined by the MOT coil current) increases, $\bar{\theta}$ is observed to shift away from zero (see Fig. 2c). The measured shift of 1.7(0.3) mrad A⁻¹ corresponds to an average clock frequency shift of $\delta\omega = \overline{\theta}/T_{int} = 2\pi \times 15.7(2.8) \text{ Hz A}^{-1}$. Second-order Zeeman shifts of this magnitude require 4.0(0.8) G cm⁻¹ ${\rm A^{-1}}$ while the ${\rm ^{87}Rb}$ atoms are in the presence of the 600-mG bias field. This value is consistent with the gradient estimated from the geometry of the MOT coils. We observed no substantial increase in the width of the detection histograms (as shown in Fig. 2b) for the relatively small (approximately 1 mrad) differential phase shifts used in this work (we can explore larger shift angles in future work). These data demonstrate that this protocol can be used to measure the frequency difference between two distant entangled clocks through the observed

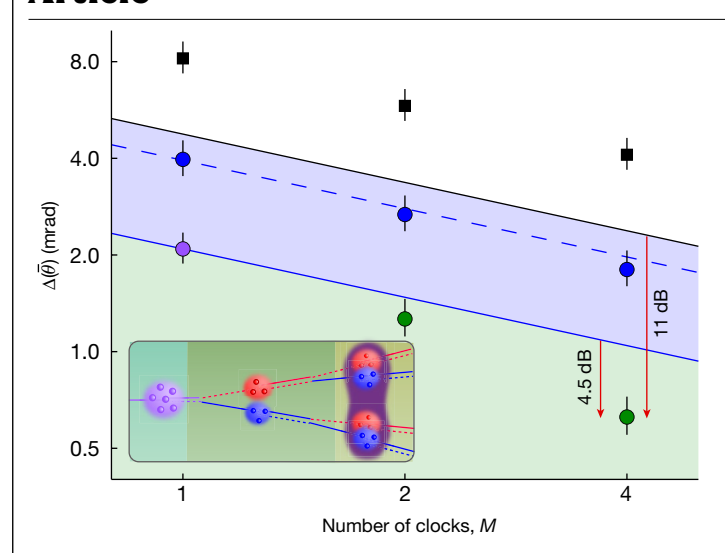


Fig. 3 | Clock network sensitivity. Measured sensitivity for a clock network utilizing SSS. The QPN limit for N = 45,000 atoms is given by the black line, which is proportional to $1/\sqrt{M}$. A mode-separable network is realized by taking independent measurements of a single-mode clock for each $\delta\theta^{(m)}$ component of $\overline{\theta}$. When observing the second QND measurement only (black squares) the sensitivity is above the QPN limit, owing to the QPN and local oscillator noise. The difference in QND measurements (blue circles) detects the spin-squeezing and brings the sensitivity below the QPN; however, the local oscillator noise remains. A one-parameter fit to these data (dashed blue line) is consistent with $1/\sqrt{M}$ scaling. Reducing the local oscillator noise would push the sensitivity lower in the blue shaded area, where the lower limit (solid blue line) is determined by the M=1 sensitivity measured without a Ramsev sequence (purple point). The mode-entangled networks (green circles) exist below this limit, where the green area represents sensitivities obtainable exclusively through simultaneous measurements of a mode-entangled network. Error bars represent the pooled variance of three sets of 200 measurements. Inset, spacetime diagram of the state preparation for a four-mode mode-entangled network.

(conditional) shift in J_z . Additional spatial modes can be added, as described below, to detect higher-order spin correlations between modes.

Next we evaluate the noise performance of entangled, multimode clock networks with N=45,000 atoms per spatial mode. The metrological improvement, relative to their respective M-mode network of N-atom coherent states, can be quantified by a parameter $\xi_{\rm net}^2$ derived from the generalized version $\xi_{\rm net}^3$ 0 of the Wineland squeezing parameter. For example, when $\xi_{\rm net}^3$ 1 of the Wineland squeezing parameter.

$$\xi_{\text{net}}^{2} = \frac{1}{C^{2}} \frac{\text{Var}(\delta J_{z}^{(1)} + \delta J_{z}^{(2)})}{\text{Var}(\delta J_{z}^{(1),CSS}) + \text{Var}(\delta J_{z}^{(2),CSS})},$$
 (2)

where the CSS variances are N/4 (see Methods). This parameter accounts for both the spatially localized and spatially distributed entanglement since $\text{Var}\left(\delta J_z^{(2)} + \delta J_z^{(1)}\right)$ is the sum of both individual variances and the covariance between the two modes.

A two-mode SSS is prepared and a pair of $\pi/2$ microwave pulses separated by a time $T_{\rm int}=100~\mu s$ constitute a standard Ramsey sequence (for simplicity, no magnetic field gradients or artificial phase shifts are present, although they could be added in principle). Squeezing reduces the variance of the joint measurement to $\Delta \bar{\theta}=1.3(0.1)$ mrad (as shown in Fig. 3), which corresponds to $\xi_{\rm net}^2=-8.6(1.0)$ dB. This precision is near that of a two-mode SSS in the absence of the Ramsey sequence ($\Delta \bar{\theta}=1.2(0.1)$ mrad without technical noise from the sensor sequence). A single-mode clock, on the other hand, has 3.6(0.6) mrad of technical noise. In this differential clock configuration, low measurement variance can be achieved without the need for high-performance local oscillators,

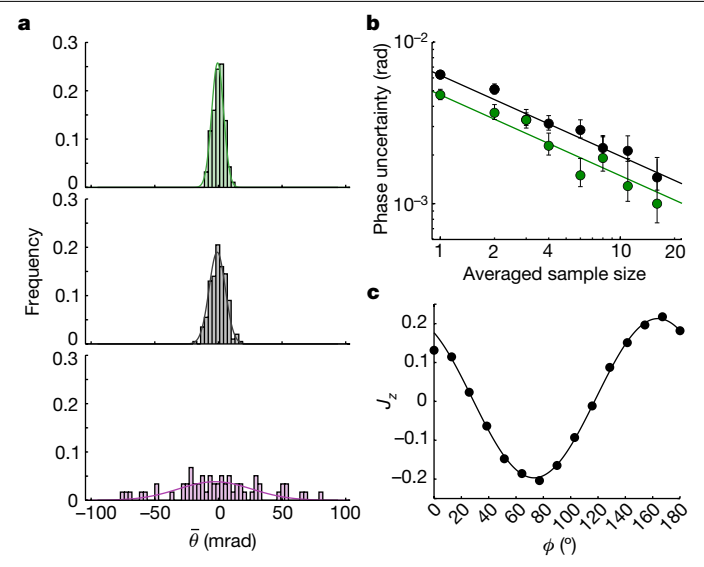


Fig. 4 | Interferometer performance. a, Distributions of 200 sample measurements for the two-mode sequence with mode-entangled squeezed states (green), mode-separable coherent states (black), and for the single-mode sequence (purple). b, The fractional stability for a two-mode interferometer with mode-entangled squeezed states (green) and mode-separable coherent states (black) is calculated from a single dataset of 200 samples. Error bars represent 68% confidence intervals. c, Response of a single-mode interferometer to a phase shift ϕ in the final Raman π pulse of the sequence. The coherence is determined from the peak-to-peak value of a sinusoidal fit.

thus circumventing a limit of previous SSS sensor demonstrations³⁴. This configuration will also suppress environmental noise common to both modes, such as a time-varying bias magnetic field. This suppression is achieved with a single collective read-out measurement.

This method can be extended to $M = 2^{P}$ clocks by further dividing the atomic ensemble with P Raman π pulses. For example, we demonstrate a four-mode system by inserting an additional Raman π pulse, followed by a microwave $\pi/2$ pulse, before the first QND measurement to generate spatially distinct modes. In this case, we adjust the total initial number of atoms to maintain N = 45,000 atoms per mode. With four modes, the metrological enhancement is $\xi_{\text{net}}^2 = 11.6(1.1) \text{ dB}$ (see Methods). For comparison, this is a 4.5(0.8)-dB relative improvement over the projected mode-separable limit (see Fig. 3). Here the network gain is driven by the improved squeezing efficiency for larger numbers of atoms, because the total number of atoms initially entangled is MN. The observed network gain is consistent with the measured atom-number dependence of squeezing efficacy observed in ref. 34 for this system (approximately 14 dB for N = 100,000). This four-mode network could be used to search, for example, for spatially periodic clock frequency shifts.

Finally, we apply this method to an atom interferometer configuration, as illustrated in Fig. 1 and Extended Data Fig. 3. In this case, two atomic spatial modes are initially spin-squeezed in an optical lattice as described above. Atoms are then released from the lattice and subject to an atom interferometer pulse sequence after an interval of approximately 7 ms, after which they have separated by about 0.16 mm. Specifically, a Raman π pulse acts as a beamsplitter by simultaneously imparting opposite momentum to the spin states in each branch (resulting in a relative momentum between interfering wavepackets of $4\hbar$ k, as depicted in Fig. 1 and Extended Data Fig. 3). $T_{\rm int}$ = 50 μ s later, a sequence of a Raman π pulse, microwave π pulse and Raman π pulse act as a mirror, and a final Raman π pulse recombines the states. The duration of the interferometer pulse sequence is 270 μ s, dominated by the approximately 160- μ s microwave π pulse time. Each mode of

N = 110,000 atoms accumulates a phase proportional to its local acceleration (see Methods). Fluorescence imaging³⁵ detects of the sum of the final $J_{\tau}^{(m)}$ (the modes are too closely spaced to resolve individually on the camera). This differential method suppresses large common mode optical phase fluctuations associated with the optical stimulated Raman transitions (measured to be 10 mrad, or roughly 15 dB above the projection noise limit, see Fig. 4a).

The smallest observed single-shot phase uncertainty with a mode-entangled interferometer is 4.9(0.4) mrad (Fig. 4b), which corresponds to an inferred differential acceleration sensitivity of 1.4(0.1) × 10⁻² m s⁻² (see Methods). This sensitivity is limited by the relatively poor contrast (40%, see Fig. 4c) associated with the interferometer pulse sequence. Entanglement-enhanced noise performance can be characterized by comparing the observed mode-entangled sensor noise to the noise observed for the same sensor sequence implemented without the entangling probe, as shown in Fig. 4a,b. With respect to the sequence that does not employ entanglement, we observe an average metrological improvement of 1.6(0.9) dB. The average absolute noise is 0.1(0.7) dB above the QPN limit for the non-entangled sensor, which we speculate is due to imperfect suppression of Raman laser phase noise. This configuration extrapolates directly to high performance, single source, differential gravity sensors (for example, ref. 11).

Conclusion

In the future, a distributed array of cavities sharing a common QND measurement²², possibly via photonic links and shared probe light^{27,39}, would enable entanglement and Bell tests across long distances. Adapting this method to squeezed optical clocks would further push the limits of precision measurements of time^{7,10} and gravity⁸. Applications in secure time transfer and quantum communications can benefit from a distributed entangled state²¹ because an eavesdropper could not deduce the correlations through observation of one clock alone. For example, information encoded by rotations on one network node would only be detectable through a collective measurement of all nodes. Finally, the atomic interferometer protocol is technologically useful for future high-performance gravity gradient sensors and differential configurations designed for gravitational wave detection 40,41 and dark matter searches 42-44.

Online content

Any methods, additional references. Nature Portfolio Reporting summaries, source data, extended data, supplementary information, acknowledgements, peer review information; details of author contributions and competing interests; and statements of data and code availability are available at https://doi.org/10.1038/s41586-022-05363-z.

- Grotti, J. et al. Geodesy and metrology with a transportable optical clock, Nat. Phys. 14. 1. 437-441 (2018).
- McGrew, W. F. et al. Atomic clock performance enabling geodesy below the centimetre level. Nature 564, 87-90 (2018).
- 3. Guo, X. et al. Distributed quantum sensing in a continuous-variable entangled network. Nat. Phys. 16, 281-284 (2020).
- Zhao, S.-R. et al. Field demonstration of distributed quantum sensing without post-selection. Phys. Rev. X 11, 031009 (2021).
- Zhang, Z. & Zhuang, Q. Distributed quantum sensing. Quantum Sci. Tech. 6, 043001
- Giovannetti, V., Lloyd, S. & Maccone, L. Quantum-enhanced positioning and clock synchronization, Nature 412, 417-419 (2001).
- Beloy, K. et al. Frequency ratio measurements at 18-digit accuracy using an optical clock network, Nature 591, 564-569 (2021).
- Bothwell, T. et al. Resolving the gravitational redshift across a millimetre-scale atomic sample. Nature 602, 420-424 (2022).
- Pedrozo-Peñafiel, E. et al. Entanglement on an optical atomic-clock transition. Nature 588, 414-418 (2020).
- Zheng, X. et al. Differential clock comparisons with a multiplexed optical lattice clock. Nature 602, 425-430 (2022).

- Overstreet, C., Asenbaum, P., Curti, J., Kim, M. & Kasevich, M. A. Observation of a gravitational Aharonov-Bohm effect. Science 375, 226-229 (2022).
- Liu, L.-Z. et al. Distributed quantum phase estimation with entangled photons. Nat. Photonics 15, 137-142 (2021).
- Xia, Y. et al. Demonstration of a reconfigurable entangled radio-frequency photonic sensor network. Phys. Rev. Lett. 124, 150502 (2020).
- Lu, H. et al. Experimental quantum network coding. npj Quantum Inf. 5, 89 (2019).
- Bodine, M. I. et al. Optical atomic clock comparison through turbulent air, Phys. Rev. Res. 2. 033395 (2020).
- Matsukevich, D. N. et al. Entanglement of remote atomic gubits, Phys. Rev. Lett. 96.
- Chou, C. W. et al. Measurement-induced entanglement for excitation stored in remote atomic ensembles. Nature 438, 828-832 (2005).
- Simon, J., Tanji, H., Ghosh, S. & Vuletić, V. Single-photon bus connecting spin-wave quantum memories. Nat. Phys. 3, 765-769 (2007).
- Muralidharan, S. et al. Optimal architectures for long distance quantum communication. Sci. Rep. 6, 20463 (2016).
- Gündoğan, M.et al. Proposal for space-borne quantum memories for global quantum networking, npi Quantum Inf. 7, 128 (2021).
- Kómár, P. et al. A quantum network of clocks, Nat. Phys. 10, 582-587 (2014).
- Polzik, E. S. & Ye, J. Entanglement and spin squeezing in a network of distant optical lattice clocks, Phys. Rev. A 93, 021404 (2016).
- Leroux, I. D., Schleier-Smith, M. H. & Vuletić, V. Orientation-dependent entanglement lifetime in a squeezed atomic clock. Phys. Rev. Lett. 104, 250801 (2010)
- 24. Gessner, M., Pezzè, L. & Smerzi, A. Sensitivity bounds for multiparameter quantum metrology. Phys. Rev. Lett. 121, 130503 (2018).
- Zhuang, Q., Zhang, Z. & Shapiro, J. H. Distributed quantum sensing using continuous-variable multipartite entanglement. Phys. Rev. A 97, 032329 (2018).
- 26. Eckert, K. et al. Differential atom interferometry beyond the standard quantum limit. Phys. Rev. A 73, 013814 (2006).
- Nichol, B. C. et al. An elementary quantum network of entangled optical atomic clocks. Nature 609, 689-694 (2022).
- Julsgaard, B., Kozhekin, A. & Polzik, E. S. Experimental long-lived entanglement of two macroscopic objects. Nature 413, 400-403 (2001).
- Fadel, M., Zibold, T., Décamps, B. & Treutlein, P. Spatial entanglement patterns and Einstein-Podolsky-Rosen steering in Bose-Einstein condensates. Science 360, 409-413 (2018).
- 30. Lange, K. et al. Entanglement between two spatially separated atomic modes, Science **360**, 416-418 (2018).
- Kunkel, P. et al. Spatially distributed multipartite entanglement enables EPR steering of atomic clouds, Science 360, 413-416 (2018).
- Anders, F. et al. Momentum entanglement for atom interferometry, Phys. Rev. Lett. 127. 140402 (2021).
- Greve. G. P., Luo, C., Wu, B. & Thompson, J. K. Entanglement-enhanced matter-wave interferometry in a high-finesse cavity. Nature 610, 472-477 (2022).
- Hosten, O., Engelsen, N. J., Krishnakumar, R. & Kasevich, M. A. Measurement noise 100 times lower than the quantum-projection limit using entangled atoms. Nature 529 505-508 (2016)
- Malia, B. K., Martínez-Rincón, J., Wu, Y., Hosten, O. & Kasevich, M. A. Free space Ramsey spectroscopy in rubidium with noise below the quantum projection limit. Phys. Rev. Lett. 125, 043202 (2020).
- Fadel, M., Yadin, B., Mao, Y., Byrnes, T. & Gessner, M. Multiparameter quantum metrology and mode entanglement with spatially split nonclassical spin states. Preprint at https:// arxiv.org/abs/2201.11081 (2022).
- Gessner, M., Smerzi, A. & Pezzè, L. Multiparameter squeezing for optimal quantum enhancements in sensor networks. Nat. Commun. 11, 3817 (2020).
- Wineland, D. J., Bollinger, J. J., Itano, W. M. & Heinzen, D. J. Squeezed atomic states and projection noise in spectroscopy. Phys. Rev. A 50, 67-88 (1994).
- Chaudhary, M. et al. Stroboscopic quantum nondemolition measurements for enhanced entanglement generation between atomic ensembles. Phys. Rev. A 105, 022443 (2022).
- Abe, M. et al. Matter-wave atomic gradiometer interferometric sensor (MAGIS-100). Quantum Sci. Tech. 6, 044003 (2021).
- Zhan, M.-S. et al. ZAIGA: Zhaoshan long-baseline atom interferometer gravitation antenna. Int. J. Mod. Phys. D 29, 1940005 (2019).
- Weisło, P. et al. New bounds on dark matter coupling from a global network of optical atomic clocks, Sci. Adv. 4, 6501 (2018).
- Safronova, M. S., Porsey, S. G., Sanner, C. & Ye, J. Two clock transitions in neutral Yb for the highest sensitivity to variations of the fine-structure constant, Phys. Rev. Lett. 120. 173001 (2018).
- Tino, G. M. Testing gravity with cold atom interferometry: results and prospects. Quantum Sci. Tech. 6, 024014 (2021).
- Jing, Y., Fadel, M., Ivannikov, V. & Byrnes, T. Split spin-squeezed Bose-Einstein condensates. New J. Phys. 21, 093038 (2019).

Publisher's note Springer Nature remains neutral with regard to jurisdictional claims in published maps and institutional affiliations.

Springer Nature or its licensor (e.g. a society or other partner) holds exclusive rights to this article under a publishing agreement with the author(s) or other rightsholder(s); author self-archiving of the accepted manuscript version of this article is solely governed by the terms of such publishing agreement and applicable law.

© The Author(s), under exclusive licence to Springer Nature Limited 2022

Methods

Contrast

When determining spatial mode separation, a second Raman pulse removes the relative momentum after time T to maintain the mode separation distance until detection takes place. A $\pi/2$ microwave pulse with varying phase addresses both modes simultaneously and the remaining contrast is determined by the peak-to-peak J_z values from fluorescence imaging (see Extended Data Fig. 2). Specifically, this is twice the amplitude of a sinusoidal fit to the data (as seen in Fig. 4c for the interferometer contrast). The coherence falls to zero after roughly one thermal de Broglie wavelength $\lambda_{\rm th} = h/\sqrt{2\pi m_{\rm Rb}k_{\rm B}T_{\rm ens}} = 36$ nm, where $k_{\rm B}$ is the Boltzmann constant, $T_{\rm ens}$ is the temperature of the ensemble, and $m_{\rm Rh}$ is the mass of the ⁸⁷Rb atom⁴⁶. This distance corresponds to 1.5 µs, at which point the contrast has reduced to less than 1%. In the absence of Raman transitions, the contrast is C = 79(1)% owing to decoherence in the lattice both before and after the sensing times. Adding in the two Raman transitions with T = 0 decreases the contrast to C = 73(1)%. Adding the magnetic field did not change the contrast by more than the margin of error (1%).

To determine C for the clock measurement, a final microwave $\pi/2$ pulse temporarily introduced to the single-mode case resolves C=78(3)%. Therefore, introducing a single Raman transition before the QND measurement does not considerably reduce the final coherence of the ensemble. The gravity gradiometer has a lower final coherence, roughly 40%, owing to four additional Raman pulses. This is consistent with the expected C=(88% population transfer)⁴ × (79% contrast without gradiometer).

Squeezing matrix for multiparameter discrete-variable squeezing

The form of the metrological squeezing parameter ξ_{net}^2 is derived from equation 13 in ref. ³⁷. For a general multimode system, the squeezing matrix Ξ^2 characterizes the level of metrological improvement due to entangled quantum network. In other words, it compares the covariances between each mode to the QPN limit. The matrix elements can be defined as

$$\Xi_{kl}^{2} = \frac{\sqrt{N^{(k)}N^{(l)}}Cov(\hat{J}_{z}^{(k)},\hat{J}_{z}^{(l)})}{\langle \hat{J}_{x}^{(k)} \rangle \langle \hat{J}_{x}^{(l)} \rangle},$$
 (3)

where $\hat{J}_{x}^{(m)}$ are the spin operators for each mode and the mean spins are in the $\hat{\mathbf{x}}$ direction.

The metrological improvement in the multiparameter estimation can be written as the ratio of variance of the squeezed network to that of a network comprised of coherent states: $\mathbf{n}^T \Sigma^2 \mathbf{n} / \mathbf{n}^T \Sigma^2_{\text{SN}} \mathbf{n}$, where Σ and Σ_{SN} are the covariance matrices of the squeezed and coherent states respectively, and \mathbf{n} is the vector of coefficients for the linear combination of parameters being measured. In the case of equally populated $(N=N^{(m)})$ modes, the expected length values are $\langle \hat{J}_x^{(m)} \rangle = CN/2$. For a measurement of the average angular shift $(n_m=1/M)$, it can be shown that the metrological improvement reduces to $\xi_{\text{net}}^2 = M\mathbf{n}^T \Xi^2\mathbf{n}$. More explicitly, in terms of the measured observables, it can be written as

$$\xi_{\text{net}}^2 = \frac{1}{C^2} \frac{\text{Var}\left(\sum_{m=1}^M \delta J_z^{(m)}\right)}{M \times \text{Var}(\delta J_z^{\text{CSS}})}.$$
 (4)

In an arbitrary network, the scaling of ξ_{net}^2 with M and N depends on the distribution of resources and the linear combination of variables used ⁴⁷.

Measurement sensitivity

Because the QND measurement addresses all modes simultaneously, it cannot distinguish between spin states with different momenta. The measured δJ_z is simply the sum of $\delta J_z^{(m)}$, with expectation value

$$\langle \delta J_z \rangle = \sum_{m=1}^M \delta J_z^{(m)} = C \frac{N}{2} \sum_{m=1}^M \delta \theta^{(m)} = C \frac{N}{2} M \overline{\theta}. \tag{5}$$

The sensitivity, σ , of this measurement to changes in $\overline{\theta}$ is given by standard error propagation³:

$$\sigma = \frac{\sqrt{\operatorname{Var}(\delta J_z)}}{\partial \langle \delta J_z \rangle / \partial \overline{\theta}} = \frac{\Delta(\delta J_z)}{CMN/2} = \Delta \overline{\theta}.$$
 (6)

Laser system

A low phase noise, 1,560-nm laser is frequency doubled to 780 nm. This light is split and one mode passes through an electro-optic modulator (EOM) driven at 6.434 GHz, 400 MHz lower than the hyperfine transition frequency, $\omega_{\rm HF}$. The driving signal is created by a low-phase-noise crystal oscillator mixed with a direct digital synthesizer, which allows for power, frequency and phase control. Next, both modes are amplified by semiconductor-based optical amplifiers to 2.8 W each.

One mode is now up-shifted by a 200-MHz acousto-optic modulator (AOM) and the other is down-shifted by the same amount. Both AOMs are driven by a common signal from a low-noise 200-MHz crystal oscillator. The pulsed signal controls the time the AOMs couple the light to optical fibres that deliver the light to the atoms. The fibres launch the light into 5.4-mm diameter, counter-propagating freespace beams at a 45° angle to the vertical and a 45° angle to the cavity axis. The shifting places one sideband of the modulated beam $\omega_{\rm HF}$ away from the unmodulated beam frequency. These two frequencies drive the Raman transition between the two hyperfine states. The two participating frequencies create a transition which is red-detuned by 3.5 GHz from the excited state. The other sidebands are used to balance the a.c. Stark shift and do not considerably contribute to the population change.

Interferometer phase shift

The sequence provided in this work differs from a standard Mach–Zehnder configuration⁴⁸ in that both spin states receive a momentum kick instead of just one state. In addition, the microwave pulses are longer than the interrogation time so terms including pulse durations must be considered. The total phase shifts, $\delta\theta^{(m)}$, of an interferometer can be derived from the sensitivity function⁴⁹:

$$\delta\theta^{(m)} = 2|\mathbf{k}|a^{(m)}(2T_{\text{int}}^2 + 4T_{\text{int}}T_0 + 4T_{\text{int}}\tau_0 + 6T_{\text{int}}\tau_k + 4T_0\tau_k + 4\tau_0\tau_k + 4\tau_k^2),$$
(7)

where $a^{(m)}$ is the acceleration in mode m projected along \mathbf{k} , $T_0 = 1$ μs is the time between sequential pulses, $\tau_0 = 80$ μs is the duration of a microwave $\pi/2$ pulse, and $\tau_k = 2$ μs is the duration of a Raman π pulse (see Extended Data Fig. 3). For the data of Fig. 4b, where $T_{\rm int} = 50$ μs , we infer a statistical sensitivity of $\Delta \overline{a} = (\sum_{m=1}^M a^{(m)})/M = 1.4(0.1) \times 10^{-2} \, \mathrm{m \, s^{-2}}$ for a single shot.

Data availability

The datasets generated and analysed during this study are available from the corresponding author upon reasonable request. Source data are provided with this paper.

Code availability

The code used for the analysis is available from the corresponding author upon reasonable request.

- Parazzoli, L. P., Hankin, A. M. & Biedermann, G. W. Observation of free-space single-atom matter wave interference. Phys. Rev. Lett. 109, 230401 (2012).
- Malitesta, M., Smerzi, A. & Pezzè, L. Distributed quantum sensing with squeezed-vacuum light in a configurable network of Mach–Zehnder interferometers Preprint at https://arxiv. org/abs/2109.09178 (2021).
- Kasevich, M. & Chu, S. Atomic interferometry using stimulated Raman transitions. Phys. Rev. Lett. 67, 181–184 (1991).
- Malia, B. K. Integration of Spin Squeezed States Into Free Space Atomic Sensors. PhD thesis, Stanford Univ. (2021).

Acknowledgements We acknowledge support from Department of Energy award DE-SC0019174-0001, the Department of Energy Q-NEXT NQI, a Vannevar Bush Faculty Fellowship and NSF QLCI Award OMA – 2016244.

Author contributions B.K.M., Y.W. and J.M.-R. designed, constructed and characterized the experiment. B.K.M. and Y.W. performed data collection and analysis. M.A.K. supervised the research. All authors contributed to the manuscript.

Competing interests M.A.K. serves as Chief Scientist, Consulting and is a shareholder of AOSense, Inc. All other authors declare no competing interests.

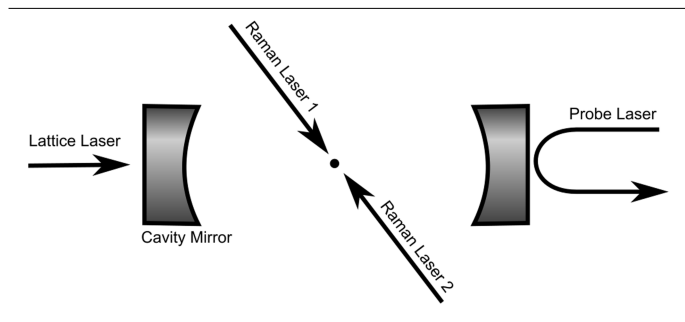
Additional information

Supplementary information The online version contains supplementary material available at https://doi.org/10.1038/s41586-022-05363-z.

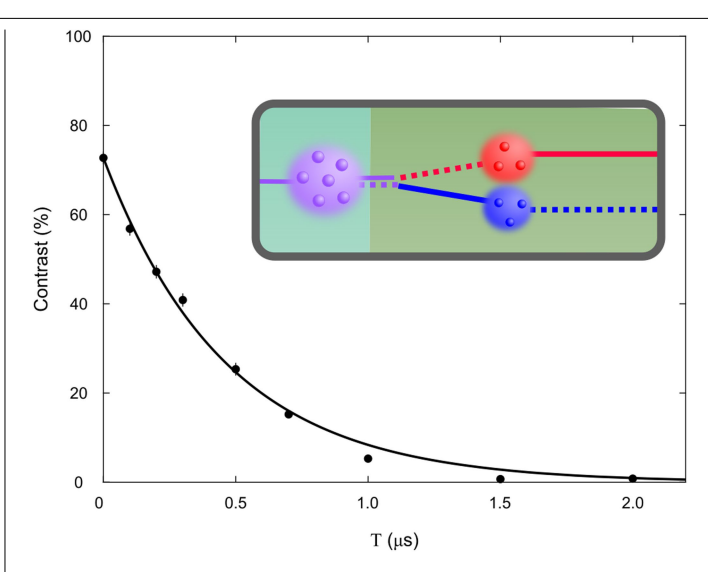
Correspondence and requests for materials should be addressed to Mark A. Kasevich.

Peer review information Nature thanks Augusto Smerzi and the other, anonymous, reviewer(s) for their contribution to the peer review of this work. Peer reviewer reports are available.

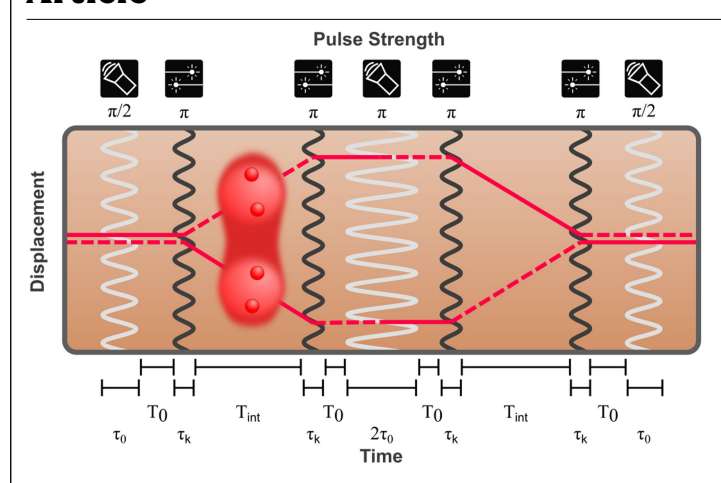
Reprints and permissions information is available at http://www.nature.com/reprints.



Extended Data Fig. 1| **Apparatus.** The atoms (black circle) are localized near the centre of the cavity. The Raman lasers enter the vacuum chamber at a 45° angle to the cavity axis. The reflected light from the probe laser is used in the homodyne detection.



Extended Data Fig. 2 | **Mode separation.** Contrast of the collective fluorescent measurement as a function of separation time between two 0.33 μ s Raman π pulses. Solid curve is an exponential fit to the data with a decay rate of 0.46 μ s. Note that T= 0 corresponds to a single pulse with a total time of 2π . Error bars represent a 95% confidence interval.



 $\label{lem:extended} \textbf{Extended Data Fig. 3} | \textbf{Interferometer sequence timing.} Space time diagram in the inertial frame of a single-mode interferometer. Solid (dashed) lines represent the trajectory of the spin down (up) state. White (grey) waves represent the finite time of the microwave (Raman) pulses.$